arXiv:1512.01493v1 [physics.atom-ph] 4 Dec 2015

Theoretical investigation of spectroscopic properties of W^{25+}

A. Alkauskas, P. Rynkun, G. Gaigalas, A. Kynienė, R. Kisielius, S. Kučas, Š. Masys, G. Merkelis, V. Jonauskas*

Institute of Theoretical Physics and Astronomy, Vilnius University, A. Goštauto 12, LT-01108 Vilnius, Lithuania

Abstract

Energy levels and emission spectra of W^{25+} ion have been studied by performing the large-scale relativistic configuration interaction calculations. Configuration interaction strength is used to determine the configurations exhibiting the largest influence on the $4f^3$, $4d^9 4f^4$, $4f^2 5s$, $4f^2 5p$, $4f^2 5d$, $4f^2 5f$, $4f^2 5g$, and $4f^2 6g$ configuration energies. It is shown that correlation effects are crucial for the $4f^2 5s \rightarrow 4f^3$ transition which in single-configuration approach occurs due to the weak electric octupole transitions. As well, the correlation effects affect the $4f^2 5d \rightarrow 4f^3$ transitions by increasing transition probabilities by an order. Corona model has been used to estimate the contribution of various transitions to the emission in a low-density electron beam ion trap (EBIT) plasma. Modeling in 10–30 nm wavelength range produces lines which do not form emission bands and can be observed in EBIT plasma.

Keywords: energy levels, radiative transition probabilities, tungsten, corona model

*Corresponding author.
Email address: Valdas.Jonauskas@tfai.vu.lt (V. Jonauskas)

1. Introduction

Tungsten features many essential properties, such as high-energy threshold of sputtering, low sputtering yield, and excellent thermal properties which make it a primary candidate for facing material of walls in thermonuclear reactors. However, some tungsten ions as impurities penetrate central regions of discharge, and their radiation takes away crucially important energy from fusion reaction. Therefore, there is a need of reliable atomic data for all tungsten ions in order to monitor the concentration of tungsten in the fusion plasma.

The aim of the current work is to study the energy levels and emission spectra of W^{25+} by performing the large-scale relativistic configuration interaction (CI) calculations. The main focus is put on the emission in the spectral range of 2–30 nm, where the intensive radiation of tungsten ions has been theoretically and experimentally investigated in fusion, electron-beam ion trap (EBIT), and laser-produced plasmas by many authors [1, 2, 3, 4, 5, 6, 7, 8, 9, 10, 11, 12, 13, 14, 15, 16, 17, 18, 19, 20]. The number of the tungsten emission studies is too large to cite here in full. Detailed reviews of available results for the tungsten spectra and spectral lines in all ionization stages are presented in [21, 22].

To the best of our knowledge, no fully relativistic with an extended CI basis theoretical investigation of emission spectra from W^{25+} ion has been carried out so far.The emission from W^{25+} has no detailed theoretical studies because of complicated calculations related to the open f shells. For ions having configurations with the open f shells, correlation effects may play a crucial role due to the mixing of large number of levels. To estimate the influence of correlation effects, the configuration interaction strength introduced previously in [23, 24] is employed in the current work. The same approach has been successfully used for the theoretical investigation of transitions in tungsten [25, 26], transition metals [27], and even the cascade of Auger processes [28, 29, 30].

The relativistic effects in the Dirac-Fock approach with quantum electrodynamic corrections have to be included to provide accurate wavelengths and radiative transition probabilities for the highly charged ions of tungsten. Previous theoretical investigations included mainly higher than W^{27+} or lower than W^{10+} ionization stages of the tungsten ions. Spectra of W^{25+} ion have been studied in [12], [13], and [16] where the pseudorelativistic approach with scaled integrals [31] is employed. In [13, 16], the configuration interaction

effects among the levels of up to three configurations are investigated. There are only a few works where energy levels and radiative transition probabilities for the tungsten ions with more than 3 electrons in f shell have been studied in the Dirac-Fock approach [32, 33].

In the following section we describe the multiconfiguration Dirac-Fock method used to calculate the energy levels and radiative transition probabilities. In Sec. III, the obtained results for the energy levels and emission spectra are discussed, and in Sec. IV, the spectra from corona model are presented and discussed.

2. Method of calculation

The multiconfiguration Dirac-Fock (MCDF) method implemented in the GRASP2K code [34] adopts the Dirac-Coulomb-Breit Hamiltonian

$$H^{\mathrm{DCB}} = \sum_i \; h_i^{\mathrm{D}} + \sum_{i<j} \; h_{ij}^{\mathrm{e}} + \sum_{i<j} \; h_{ij}^{\mathrm{trans}}, \tag{1}$$

to solve atomic structure problem for atoms and ions. Here $h_i^{\mathrm{D}} = c\alpha_i \cdot p_i + (\beta_i - 1)c^2 + V(r_i)$ is one-electron Dirac Hamiltonian, α and β are the fourth-order Dirac matrices, p is the momentum operator, $V(r_i)$ is the electrostatic electron-nucleus interaction, h_{ij}^{e} is the instantaneous Coulomb repulsion and h_{ij}^{trans} is the transverse interaction operator:

$$h_{ij}^{trans} = \frac{1}{r_{ij}} \left[1 - \alpha_i \cdot \alpha_j \;\; \cos(\omega r_{ij}) + (\alpha_i \cdot \nabla_i)(\alpha_j \cdot \nabla_j) \;\; \frac{\cos(\omega r_{ij}) - 1}{\omega^2} \right] \tag{2}$$

where ω is the energy of a single photon exchanged between a pair of electrons i and j.

Diagonalization of the Dirac-Coulomb-Breit Hamiltonian produces atomic state functions, Ψ_γ, which characterize different fine-structure states and are expressed through the configuration state functions (CSFs)

$$\Psi_\gamma(J) = \sum_\zeta c_\gamma(\zeta J) \;\; \Phi(\zeta J), \tag{3}$$

where ζ represents any additional quantum numbers required to uniquely specify a state. The CSFs, $\Phi(\zeta J)$, are built from a basis of two-component orbitals

$$\phi(r) = \frac{1}{r} \begin{pmatrix} P_{nlj}(r) & \chi_{ljm}(\hat{r}) \\ \mathrm{i}\; Q_{n\bar{l}j}(r) & \chi_{\bar{l}jm}(\hat{r}) \end{pmatrix}. \tag{4}$$

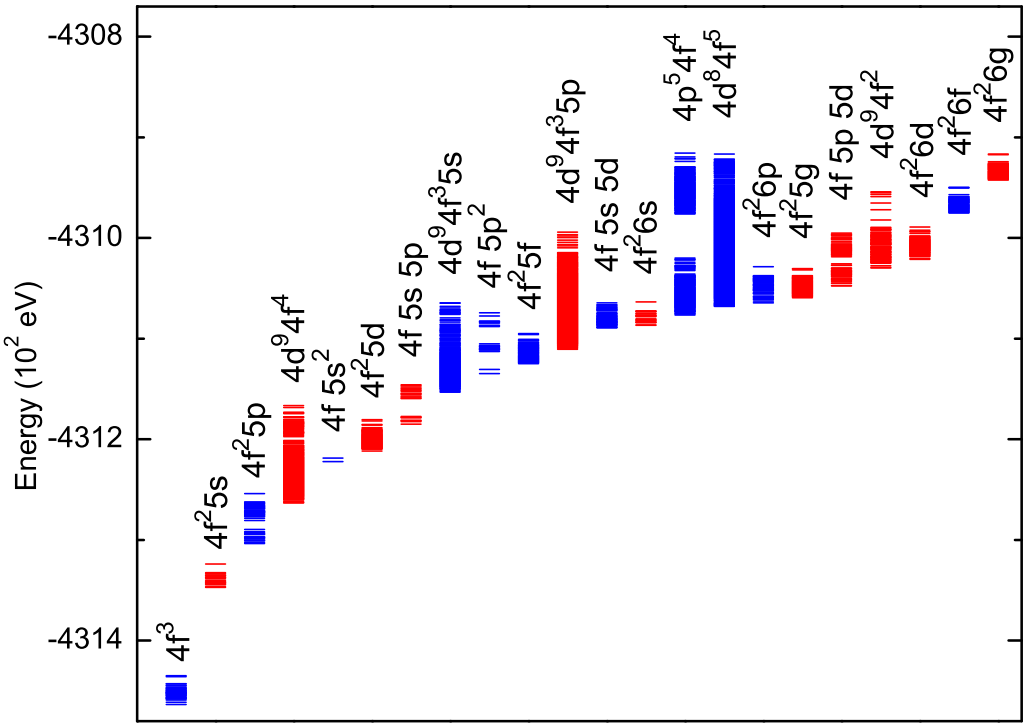

Figure 1: Energy levels of studied configurations in W^{25+}.

Here $P_{nlj}(r)$ and $Q_{n\bar{l}j}(r)$ are the large and small radial components of one-electron wavefunctions and $\chi_{ljm}(\hat{r})$ are the two-component Pauli spherical spinors.

QED corrections, which include vacuum polarization and self-energy (known as the Lamb shift), are considered in the first order of perturbation theory. Finally, the effects of finite nuclear size are modeled by using two-component Fermi statistical distribution function.

3. Energy levels and radiative transition probabilities

Theoretical energy levels for 22 configurations of W^{25+} are presented in Figure 1. The levels are identified by their dominant components in the LS coupled basis set. We include all the configurations which have energy levels either lower or overlaping with the highest energy level of $4d^9 4f^3 5s$ configuration. In addition, the configurations which correspond to the one-electron excitations from the ground $4f^3$ configuration up to $6g$ shell are also pre-

sented. The configuration $4d^9 4f^3 5s$ originates from the ground configuration $4f^3$ of the ion after the one-electron excitation from the $4d$ to $5s$ shell. The total number of levels in the present work equals to 13937. The ground configuration of the ion consists of 41 levels (Table 1). It can be seen from Table 1 that a mixing among the configuration state functions in LS-coupling is very prominent for some levels of the ground configuration. On the other hand, our expansion coefficients for the atomic wavefunctions in jj-coupling (not presented here) show that none of the coupling schemes are suitable for the unique identification of some levels.

The first excited configuration $4f^2 5s$ can decay to the ground configuration only through the electric octupole transitions in single-configuration approach. The largest probabilities for these transitions are of 10 s^{-1} order, and the transitions concentrate in the 10–12 nm region. Configuration mixing opens decay channels for electric dipole transitions to the levels of the ground configuration. However, their probabilities are much weaker compared to the other considered electric dipole transitions. The largest transition probabilities are of 10^7 s^{-1} order. The analysis of percentage compositions of the configuration state functions for levels reveals that the mixing of $4f^2 5s$ with $4d^9 4f^4$, $4f^2 5d$, and $4d^9 4f^3 5p$ configurations is responsible for the electric dipole transitions. However, the percentage composition of the configuration state functions from these three configurations does not reach more than 1%. It should be noted that a very large CI basis is needed for such a small mixing of the configuration state functions in order to provide the reliable values of the radiative transition probabilities. The lines from $4f^2 5s \rightarrow 4f^3$ transition appear in the spectra when the population of the higher levels goes down through the steps of radiative transitions. Likewise, such process can appear on the scene in EBIT plasma when the interaction with electrons ends for ions ejected from electron beam [35] or in magnetic trapping mode [36]. The charge exchange of the ions with neutrals can also result in the radiative cascade of transferred electrons from the highly excited states of the ions [37, 38].

Table 1: MCDF energy levels with spectroscopic identifications and leading percentage composition of the wave functions in W^{25+}. Levels having the largest lifetimes and levels to which radiative transition takes place from these levels are presented. JP stands for the total angular momentum quantum number J and parity P. Energies are given relative to the ground energy $E_{ground} = -15855.9891992$ a.u.

Index	JP	E (a.u.)	Composition
1	9/2−	E_{ground}	82% $4f^3$ ($^4_1$I) ^{4}I + 14% $4f^3$ ($^2_2$H) ^{2}H + 2% $4f^3$ ($^2_1$H) ^{2}H + 1% $4f^3$ ($^2_1$G) ^{2}G + 1% $4f^3$ ($^2_2$G) ^{2}G
2	11/2−	0.0902578	94% $4f^3$ ($^4_1$I) ^{4}I + 4% $4f^3$ ($^2_2$H) ^{2}H + 1% $4f^3$ ($^2_1$H) ^{2}H
3	3/2−	0.1632922	64% $4f^3$ ($^4_1$F) ^{4}F + 22% $4f^3$ ($^2_1$D) ^{2}D + 7% $4f^3$ ($^2_1$P) ^{2}P + 3% $4f^3$ ($^2_2$D) ^{2}D + 3% $4f^3$ ($^4_1$S) ^{4}S
4	13/2−	0.1677164	92% $4f^3$ ($^4_1$I) ^{4}I + 6% $4f^3$ ($^2_1$K) ^{2}K + 1% $4f^3$ ($^2_1$I) ^{2}I
5	9/2−	0.2012862	33% $4f^3$ ($^2_2$H) ^{2}H + 19% $4f^3$ ($^2_1$G) ^{2}G + 14% $4f^3$ ($^2_2$G) ^{2}G + 13% $4f^3$ ($^4_1$I) ^{4}I + 11% $4f^3$ ($^4_1$F) ^{4}F
6	5/2−	0.2240156	77% $4f^3$ ($^4_1$F) ^{4}F + 10% $4f^3$ ($^2_1$D) ^{2}D + 8% $4f^3$ ($^4_1$G) ^{4}G + 2% $4f^3$ ($^2_1$F) ^{2}F + 2% $4f^3$ ($^2_2$F) ^{2}F
7	15/2−	0.2350187	82% $4f^3$ ($^4_1$I) ^{4}I + 16% $4f^3$ ($^2_1$K) ^{2}K + 1% $4f^3$ ($^2_1$L) ^{2}L
8	3/2−	0.2488323	63% $4f^3$ ($^4_1$S) ^{4}S + 22% $4f^3$ ($^2_1$P) ^{2}P + 13% $4f^3$ ($^4_1$F) ^{4}F + 1% $4f^3$ ($^4_1$D) ^{4}D + 1% $4f^3$ ($^2_1$D) ^{2}D
9	7/2−	0.2506589	50% $4f^3$ ($^4_1$F) ^{4}F + 25% $4f^3$ ($^2_1$G) ^{2}G + 17% $4f^3$ ($^2_2$G) ^{2}G + 6% $4f^3$ ($^4_1$G) ^{4}G + 1% $4f^3$ ($^2_2$F) ^{2}F
10	5/2−	0.2631267	80% $4f^3$ ($^4_1$G) ^{4}G + 10% $4f^3$ ($^4_1$F) ^{4}F + 4% $4f^3$ ($^2_1$F) ^{2}F + 3% $4f^3$ ($^2_2$F) ^{2}F + 1% $4f^3$ ($^2_2$D) ^{2}D
11	7/2−	0.3041443	63% $4f^3$ ($^4_1$G) ^{4}G + 25% $4f^3$ ($^4_1$F) ^{4}F + 4% $4f^3$ ($^2_2$G) ^{2}G + 4% $4f^3$ ($^2_1$G) ^{2}G + 2% $4f^3$ ($^2_2$F) ^{2}F
12	9/2−	0.3189015	61% $4f^3$ ($^4_1$F) ^{4}F + 26% $4f^3$ ($^2_2$H) ^{2}H + 6% $4f^3$ ($^2_1$G) ^{2}G + 3% $4f^3$ ($^4_1$I) ^{4}I + 1% $4f^3$ ($^2_2$G) ^{2}G
13	11/2−	0.3290696	66% $4f^3$ ($^2_2$H) ^{2}H + 19% $4f^3$ ($^4_1$G) ^{4}G + 5% $4f^3$ ($^2_1$H) ^{2}H + 4% $4f^3$ ($^4_1$I) ^{4}I + 4% $4f^3$ ($^2_1$I) ^{2}I
14	13/2−	0.3360449	88% $4f^3$ ($^2_1$K) ^{2}K + 7% $4f^3$ ($^4_1$I) ^{4}I + 4% $4f^3$ ($^2_1$I) ^{2}I
15	3/2−	0.3656872	24% $4f^3$ ($^4_1$S) ^{4}S + 21% $4f^3$ ($^2_1$D) ^{2}D + 16% $4f^3$ ($^4_1$F) ^{4}F + 14% $4f^3$ ($^4_1$D) ^{4}D + 14% $4f^3$ ($^2_1$P) ^{2}P
16	7/2−	0.3677222	29% $4f^3$ ($^2_1$G) ^{2}G + 27% $4f^3$ ($^4_1$G) ^{4}G + 23% $4f^3$ ($^4_1$F) ^{4}F + 19% $4f^3$ ($^2_2$G) ^{2}G + 1% $4f^3$ ($^2_2$F) ^{2}F
17	1/2−	0.3811356	65% $4f^3$ ($^2_1$P) ^{2}P + 33% $4f^3$ ($^4_1$D) ^{4}D
18	9/2−	0.3813196	84% $4f^3$ ($^4_1$G) ^{4}G + 7% $4f^3$ ($^2_1$H) ^{2}H + 5% $4f^3$ ($^2_2$H) ^{2}H + 1% $4f^3$ ($^2_2$G) ^{2}G + 1% $4f^3$ ($^4_1$I) ^{4}I
19	15/2−	0.3974398	49% $4f^3$ ($^2_1$K) ^{2}K + 36% $4f^3$ ($^2_1$L) ^{2}L + 14% $4f^3$ ($^4_1$I) ^{4}I
20	5/2−	0.4100329	30% $4f^3$ ($^4_1$D) ^{4}D + 29% $4f^3$ ($^2_2$D) ^{2}D + 26% $4f^3$ ($^2_1$D) ^{2}D + 4% $4f^3$ ($^4_1$F) ^{4}F + 4% $4f^3$ ($^4_1$G) ^{4}G
21	11/2−	0.4298672	46% $4f^3$ ($^2_1$H) ^{2}H + 35% $4f^3$ ($^4_1$G) ^{4}G + 13% $4f^3$ ($^2_1$I) ^{2}I + 4% $4f^3$ ($^2_2$H) ^{2}H + 1% $4f^3$ ($^4_1$I) ^{4}I
22	3/2−	0.4419216	46% $4f^3$ ($^4_1$D) ^{4}D + 26% $4f^3$ ($^2_2$D) ^{2}D + 12% $4f^3$ ($^2_1$D) ^{2}D + 10% $4f^3$ ($^2_1$P) ^{2}P + 4% $4f^3$ ($^4_1$S) ^{4}S
23	5/2−	0.4485547	59% $4f^3$ ($^2_1$D) ^{2}D + 26% $4f^3$ ($^4_1$D) ^{4}D + 6% $4f^3$ ($^4_1$F) ^{4}F + 4% $4f^3$ ($^2_2$D) ^{2}D + 1% $4f^3$ ($^2_2$F) ^{2}F
24	9/2−	0.4659291	33% $4f^3$ ($^2_1$G) ^{2}G + 25% $4f^3$ ($^4_1$F) ^{4}F + 17% $4f^3$ ($^2_2$H) ^{2}H + 17% $4f^3$ ($^2_2$G) ^{2}G + 5% $4f^3$ ($^2_1$H) ^{2}H
25	11/2−	0.4768551	58% $4f^3$ ($^2_1$I) ^{2}I + 35% $4f^3$ ($^4_1$G) ^{4}G + 3% $4f^3$ ($^2_2$H) ^{2}H + 3% $4f^3$ ($^2_1$H) ^{2}H
26	1/2−	0.4989921	65% $4f^3$ ($^4_1$D) ^{4}D + 33% $4f^3$ ($^2_1$P) ^{2}P
27	3/2−	0.5203918	30% $4f^3$ ($^2_1$P) ^{2}P + 24% $4f^3$ ($^2_1$D) ^{2}D + 21% $4f^3$ ($^2_2$D) ^{2}D + 15% $4f^3$ ($^4_1$D) ^{4}D + 5% $4f^3$ ($^4_1$S) ^{4}S
28	13/2−	0.5316025	94% $4f^3$ ($^2_1$I) ^{2}I + 5% $4f^3$ ($^2_1$K) ^{2}K
29	7/2−	0.5316294	91% $4f^3$ ($^4_1$D) ^{4}D + 5% $4f^3$ ($^2_1$F) ^{2}F + 1% $4f^3$ ($^2_2$F) ^{2}F + 1% $4f^3$ ($^4_1$G) ^{4}G + 1% $4f^3$ ($^2_1$G) ^{2}G
30	15/2−	0.5341773	62% $4f^3$ ($^2_1$L) ^{2}L + 34% $4f^3$ ($^2_1$K) ^{2}K + 2% $4f^3$ ($^4_1$I) ^{4}I
31	9/2−	0.5486678	74% $4f^3$ ($^2_1$H) ^{2}H + 13% $4f^3$ ($^2_2$G) ^{2}G + 6% $4f^3$ ($^4_1$G) ^{4}G + 4% $4f^3$ ($^2_2$H) ^{2}H + 1% $4f^3$ ($^4_1$F) ^{4}F
32	17/2−	0.5545060	99% $4f^3$ ($^2_1$L) ^{2}L
33	5/2−	0.5863249	33% $4f^3$ ($^4_1$D) ^{4}D + 30% $4f^3$ ($^2_2$F) ^{2}F + 20% $4f^3$ ($^2_1$F) ^{2}F + 9% $4f^3$ ($^2_2$D) ^{2}D + 5% $4f^3$ ($^4_1$G) ^{4}G
34	3/2−	0.6041386	39% $4f^3$ ($^2_2$D) ^{2}D + 23% $4f^3$ ($^4_1$D) ^{4}D + 19% $4f^3$ ($^2_1$D) ^{2}D + 16% $4f^3$ ($^2_1$P) ^{2}P + 1% $4f^3$ ($^4_1$S) ^{4}S
35	11/2−	0.6294527	44% $4f^3$ ($^2_1$H) ^{2}H + 24% $4f^3$ ($^2_1$I) ^{2}I + 21% $4f^3$ ($^2_2$H) ^{2}H + 9% $4f^3$ ($^4_1$G) ^{4}G
36	7/2−	0.6883423	65% $4f^3$ ($^2_2$F) ^{2}F + 21% $4f^3$ ($^2_1$F) ^{2}F + 6% $4f^3$ ($^4_1$D) ^{4}D + 4% $4f^3$ ($^2_1$G) ^{2}G + 2% $4f^3$ ($^4_1$G) ^{4}G
37	5/2−	0.6932423	56% $4f^3$ ($^2_2$D) ^{2}D + 17% $4f^3$ ($^2_1$F) ^{2}F + 13% $4f^3$ ($^2_2$F) ^{2}F + 10% $4f^3$ ($^4_1$D) ^{4}D + 2% $4f^3$ ($^4_1$G) ^{4}G
38	9/2−	0.7512285	52% $4f^3$ ($^2_2$G) ^{2}G + 40% $4f^3$ ($^2_1$G) ^{2}G + 5% $4f^3$ ($^2_1$H) ^{2}H + 1% $4f^3$ ($^2_2$H) ^{2}H
39	7/2−	0.7696339	53% $4f^3$ ($^2_2$G) ^{2}G + 35% $4f^3$ ($^2_1$G) ^{2}G + 8% $4f^3$ ($^2_2$F) ^{2}F + 2% $4f^3$ ($^2_1$F) ^{2}F
40	7/2−	1.0247182	69% $4f^3$ ($^2_1$F) ^{2}F + 21% $4f^3$ ($^2_2$F) ^{2}F + 4% $4f^3$ ($^2_2$G) ^{2}G + 2% $4f^3$ ($^2_1$G) ^{2}G + 2% $4f^3$ ($^4_1$D) ^{4}D
41	5/2−	1.0572781	52% $4f^3$ ($^2_1$F) ^{2}F + 46% $4f^3$ ($^2_2$F) ^{2}F

Continued on next page

Table 1: (continued)

Index	JP	E (a.u.)	Composition
163	19/2+	7.6177821	42% $4d^9\ 4f^4\ (^5_1I)\ ^6K$ + 34% $4d^9\ 4f^4\ (^5_1I)\ ^6L$ + 6% $4d^9\ 4f^4\ (^3_2K)\ ^4L$ + 6% $4d^9\ 4f^4\ (^3_2K)\ ^4M$ + 2% $4d^9\ 4f^4\ (^3_1K)\ ^4M$
172	21/2+	7.6626000	56% $4d^9\ 4f^4\ (^5_1I)\ ^6L$ + 24% $4d^9\ 4f^4\ (^3_2K)\ ^4M$ + 5% $4d^9\ 4f^4\ (^3_1L)\ ^4N$ + 5% $4d^9\ 4f^4\ (^3_1K)\ ^4M$ + 5% $4d^9\ 4f^4\ (^1_2L)\ ^2N$
199	19/2+	7.7465147	20% $4d^9\ 4f^4\ (^5_1I)\ ^6L$ + 18% $4d^9\ 4f^4\ (^3_1L)\ ^4N$ + 9% $4d^9\ 4f^4\ (^3_1L)\ ^4M$ + 8% $4d^9\ 4f^4\ (^3_1L)\ ^2N$ + 7% $4d^9\ 4f^4\ (^3_1K)\ ^4M$
204	21/2+	7.7558985	27% $4d^9\ 4f^4\ (^5_1I)\ ^6L$ + 19% $4d^9\ 4f^4\ (^3_1L)\ ^4N$ + 17% $4d^9\ 4f^4\ (^3_1M)\ ^4O$ + 14% $4d^9\ 4f^4\ (^3_1M)\ ^2O$ + 11% $4d^9\ 4f^4\ (^1_2L)\ ^2N$
222	23/2+	7.8064391	44% $4d^9\ 4f^4\ (^3_1M)\ ^4O$ + 42% $4d^9\ 4f^4\ (^3_1L)\ ^4N$ + 9% $4d^9\ 4f^4\ (^3_1M)\ ^2O$ + 6% $4d^9\ 4f^4\ (^3_1M)\ ^4N$
242	21/2+	7.8498415	29% $4d^9\ 4f^4\ (^3_1L)\ ^4N$ + 23% $4d^9\ 4f^4\ (^1_2L)\ ^2N$ + 16% $4d^9\ 4f^4\ (^3_1M)\ ^2O$ + 11% $4d^9\ 4f^4\ (^3_1L)\ ^4M$ + 6% $4d^9\ 4f^4\ (^3_1K)\ ^4M$
248	25/2+	7.8577952	88% $4d^9\ 4f^4\ (^3_1M)\ ^4O$ + 12% $4d^9\ 4f^4\ (^1_1N)\ ^2Q$
255	19/2+	7.8735085	28% $4d^9\ 4f^4\ (^3_1I)\ ^4L$ + 22% $4d^9\ 4f^4\ (^3_2K)\ ^4L$ + 13% $4d^9\ 4f^4\ (^3_1L)\ ^4N$ + 11% $4d^9\ 4f^4\ (^3_1L)\ ^2N$ + 6% $4d^9\ 4f^4\ (^5_1I)\ ^6K$
260	21/2+	7.8851464	38% $4d^9\ 4f^4\ (^3_2K)\ ^4M$ + 16% $4d^9\ 4f^4\ (^3_1M)\ ^4O$ + 14% $4d^9\ 4f^4\ (^5_1I)\ ^6L$ + 13% $4d^9\ 4f^4\ (^3_1M)\ ^2O$ + 10% $4d^9\ 4f^4\ (^1_2L)\ ^2N$
270	19/2+	7.8984569	28% $4d^9\ 4f^4\ (^3_2K)\ ^4M$ + 11% $4d^9\ 4f^4\ (^1_2L)\ ^2M$ + 11% $4d^9\ 4f^4\ (^3_2K)\ ^2M$ + 7% $4d^9\ 4f^4\ (^3_1M)\ ^4N$ + 6% $4d^9\ 4f^4\ (^1_1K)\ ^2M$
284	23/2+	7.9247134	47% $4d^9\ 4f^4\ (^3_1L)\ ^4N$ + 32% $4d^9\ 4f^4\ (^3_1M)\ ^4O$ + 17% $4d^9\ 4f^4\ (^3_1M)\ ^2O$ + 4% $4d^9\ 4f^4\ (^3_1M)\ ^4N$
297	21/2+	7.9484240	26% $4d^9\ 4f^4\ (^3_1L)\ ^4M$ + 19% $4d^9\ 4f^4\ (^3_1L)\ ^2N$ + 14% $4d^9\ 4f^4\ (^3_1K)\ ^4M$ + 10% $4d^9\ 4f^4\ (^3_1M)\ ^4M$ + 9% $4d^9\ 4f^4\ (^3_1L)\ ^4N$
331	19/2+	8.0053795	16% $4d^9\ 4f^4\ (^3_2K)\ ^4L$ + 10% $4d^9\ 4f^4\ (^3_1M)\ ^4N$ + 10% $4d^9\ 4f^4\ (^3_1L)\ ^4N$ + 8% $4d^9\ 4f^4\ (^3_2K)\ ^2M$ + 6% $4d^9\ 4f^4\ (^3_1M)\ ^4M$
348	21/2+	8.0334675	36% $4d^9\ 4f^4\ (^1_2L)\ ^2N$ + 20% $4d^9\ 4f^4\ (^3_1M)\ ^2O$ + 13% $4d^9\ 4f^4\ (^3_1M)\ ^4N$ + 13% $4d^9\ 4f^4\ (^3_2K)\ ^4M$ + 5% $4d^9\ 4f^4\ (^3_1K)\ ^4M$
350	25/2+	8.0341442	88% $4d^9\ 4f^4\ (^1_1N)\ ^2Q$ + 12% $4d^9\ 4f^4\ (^3_1M)\ ^4O$
366	23/2+	8.0573172	60% $4d^9\ 4f^4\ (^3_1M)\ ^4N$ + 16% $4d^9\ 4f^4\ (^3_1M)\ ^2O$ + 11% $4d^9\ 4f^4\ (^3_1L)\ ^4N$ + 5% $4d^9\ 4f^4\ (^1_1N)\ ^2O$ + 4% $4d^9\ 4f^4\ (^3_1M)\ ^4O$
368	21/2+	8.0595059	22% $4d^9\ 4f^4\ (^3_1M)\ ^4N$ + 15% $4d^9\ 4f^4\ (^3_1K)\ ^4M$ + 12% $4d^9\ 4f^4\ (^3_2K)\ ^4M$ + 11% $4d^9\ 4f^4\ (^3_1M)\ ^4O$ + 11% $4d^9\ 4f^4\ (^1_1L)\ ^2N$
392	21/2+	8.0981039	38% $4d^9\ 4f^4\ (^3_1L)\ ^4M$ + 12% $4d^9\ 4f^4\ (^3_1K)\ ^4M$ + 11% $4d^9\ 4f^4\ (^3_1M)\ ^4N$ + 11% $4d^9\ 4f^4\ (^1_1L)\ ^2N$ + 7% $4d^9\ 4f^4\ (^1_2L)\ ^2N$
493	23/2+	8.2522591	50% $4d^9\ 4f^4\ (^1_1N)\ ^2O$ + 40% $4d^9\ 4f^4\ (^1_1N)\ ^2Q$ + 8% $4d^9\ 4f^4\ (^3_1M)\ ^4N$ + 1% $4d^9\ 4f^4\ (^3_1M)\ ^2O$
4130	27/2−	14.9956274	33% $4d^8\ (^3_2F)\ ^3F\ 4f^5\ (^4_0M)\ ^6O$ + 27% $4d^8\ (^3_2F)\ ^3F\ 4f^5\ (^4_0M)\ ^6Q$ + 23% $4d^8\ (^3_2F)\ ^3F\ 4f^5\ (^4_1L)\ ^6O$ + 3% $4d^8\ (^1_2G)\ ^1G\ 4f^5\ (^4_0M)\ ^4Q$ + 3% $4d^8\ (^3_2F)\ ^3F\ 4f^5\ (^2_1N)\ ^4Q$
4247	29/2−	15.0375603	76% $4d^8\ (^3_2F)\ ^3F\ 4f^5\ (^4_0M)\ ^6Q$ + 14% $4d^8\ (^3_2F)\ ^3F\ 4f^5\ (^2_1N)\ ^4R$ + 7% $4d^8\ (^1_2G)\ ^1G\ 4f^5\ (^4_0M)\ ^4R$ + 2% $4d^8\ (^1_2G)\ ^1G\ 4f^5\ (^2_1N)\ ^2T$ + 1% $4d^8\ (^3_2F)\ ^3F\ 4f^5\ (^2_0O)\ ^2T$
4796	29/2−	15.2300106	38% $4d^8\ (^3_2F)\ ^3F\ 4f^5\ (^2_1N)\ ^4R$ + 18% $4d^8\ (^3_2F)\ ^3F\ 4f^5\ (^2_0O)\ ^4T$ + 14% $4d^8\ (^3_2F)\ ^3F\ 4f^5\ (^2_0O)\ ^2T$ + 13% $4d^8\ (^3_2F)\ ^3F\ 4f^5\ (^4_0M)\ ^6Q$ + 7% $4d^8\ (^1_2G)\ ^1G\ 4f^5\ (^2_1N)\ ^2T$
4956	31/2−	15.2822190	86% $4d^8\ (^3_2F)\ ^3F\ 4f^5\ (^2_0O)\ ^4T$ + 14% $4d^8\ (^1_2G)\ ^1G\ 4f^5\ (^2_0O)\ ^2U$

Table 2: Configuration interaction strengths T between initial K_1 and admixed K_2 configurations divided by statistical weight g_1 of initial configuration for some configurations in W^{25+}. Shells of admixed configurations K_2 marked relatively to the corresponding initial configuration K_1.

K_1	T/g_1	K_2	T/g_1	K_2	T/g_1	K_2	T/g_1	K_2
$4f^3$	1.26−2	$4d^{-2}4f^2$	5.95−3	$4d^{-1}5d^1$	2.30−3	$4f^{-1}5f^1$	1.96−3	$4p^{-1}5p^1$
	1.52−3	$4d^{-1}5g^1$	9.23−4	$4p^{-1}4f^1$	8.06−4	$4d^{-1}6d^1$	6.61−4	$4d^{-1}6g^1$
	4.45−4	$4s^{-1}5s^1$	4.27−4	$4p^{-2}4f^2$	3.30−4	$4d^{-1}7g^1$	3.07−4	$4f^{-1}6f^1$
	3.05−4	$4d^{-2}5d^2$	3.04−4	$4p^{-1}4d^{-1}4f^15g^1$	2.92−4	$4p^{-1}4d^{-1}5p^15d^1$	2.91−4	$4d^{-1}4f^{-1}5d^15f^1$
	2.58−4	$4p^{-1}6p^1$	2.55−4	$4d^{-1}7d^1$	1.62−4	$4p^{-1}4d^{-1}4f^16g^1$	1.49−4	$4d^{-2}5d^16d^1$
$4d^94f^4$	8.48−3	$4d^{-1}5d^1$	8.41−3	$4d^{-2}4f^2$	7.05−3	$4d^14f^{-2}5d^1$	6.67−3	$4f^{-1}5f^1$
	3.69−3	$4p^{-1}4f^1$	3.08−3	$4p^{-1}5p^1$	1.75−3	$4d^{-1}5g^1$	1.14−3	$4d^{-1}6d^1$
	8.86−4	$4f^{-1}6f^1$	7.62−4	$4d^{-1}6g^1$	6.99−4	$4s^{-1}5s^1$	5.33−4	$4d^14f^{-2}5g^1$
	4.04−4	$4p^{-1}6p^1$	3.81−4	$4d^{-1}7g^1$	3.62−4	$4d^{-1}7d^1$	3.51−4	$4d^{-1}4f^{-1}5d^15f^1$
	3.50−4	$4p^{-2}4f^2$	2.72−4	$4f^{-1}7f^1$	2.66−4	$4p^{-1}4d^{-1}5p^15d^1$	2.49−4	$4p^{-1}4d^{-1}4f^15g^1$
$4f^25s$	1.52−2	$4d^{-2}4f^2$	5.63−3	$4d^{-1}4f^15s^{-1}5p^1$	4.43−3	$4d^{-1}5d^1$	1.49−3	$4p^{-1}5p^1$
	1.06−3	$4d^{-1}5g^1$	7.41−4	$4p^{-1}4f^1$	5.85−4	$4d^{-1}6d^1$	5.28−4	$4f^{-1}5f^1$
	5.23−4	$5s^{-1}5d^1$	5.12−4	$4p^{-2}4f^2$	4.61−4	$4d^{-1}6g^1$	3.24−4	$4p^{-1}4d^{-1}4f^15g^1$
	2.92−4	$4d^{-2}5d^2$	2.82−4	$4p^{-1}4d^{-1}5p^15d^1$	2.31−4	$4d^{-1}7g^1$	2.16−4	$4d^{-1}4f^15s^{-1}6p^1$
	1.96−4	$4f^{-1}5s^{-1}5p^15g^1$	1.87−4	$4p^{-1}6p^1$	1.84−4	$4d^{-1}7d^1$	1.84−4	$4d^{-1}4f^{-1}5d^15f^1$
$4f^25p$	1.52−2	$4d^{-2}4f^2$	5.28−3	$4d^{-1}4f^15s^15p^{-1}$	4.38−3	$4d^{-1}5d^1$	2.85−3	$4d^{-1}4f^15p^{-1}5d^1$
	1.20−3	$4p^{-1}5p^1$	1.11−3	$4d^{-1}5g^1$	8.61−4	$4p^{-1}4f^1$	5.78−4	$4d^{-1}6d^1$
	5.19−4	$4f^{-1}5f^1$	5.12−4	$4p^{-2}4f^2$	4.77−4	$4d^{-1}6g^1$	3.26−4	$4s^{-1}5s^1$
	3.23−4	$4p^{-1}4d^{-1}4f^15g^1$	2.91−4	$4d^{-2}5d^2$	2.38−4	$4d^{-1}7g^1$	2.34−4	$4p^{-1}4d^{-1}5p^15d^1$
	1.96−4	$4p^{-1}6p^1$	1.84−4	$5p^{-1}5f^1$	1.83−4	$4d^{-1}4f^{-1}5d^15f^1$	1.83−4	$4d^{-1}7d^1$
$4f^25d$	7.76−2	$4d^{-1}4f^25d^{-1}$	1.52−2	$4d^{-2}4f^2$	7.10−3	$4d^{-1}4f^15p^15d^{-1}$	3.86−3	$4d^{-1}5d^1$
	2.05−3	$4d^{-1}4f^15d^{-1}5f^1$	1.42−3	$4p^{-1}5p^1$	1.09−3	$4d^{-1}5g^1$	8.31−4	$4p^{-1}4f^1$
	6.02−4	$4d^{-1}6d^1$	5.13−4	$4p^{-2}4f^2$	5.10−4	$4f^{-1}5f^1$	4.69−4	$4d^{-1}6g^1$
	3.51−4	$4f^{-1}5s^15p^15d^{-1}$	3.23−4	$4p^{-1}4d^{-1}4f^15g^1$	3.22−4	$4s^{-1}5s^1$	2.52−4	$4p^{-1}4d^{-1}5p^15d^1$
	2.34−4	$4d^{-1}7g^1$	2.32−4	$4d^{-2}5d^2$	1.93−4	$4d^{-1}7d^1$	1.85−4	$4p^{-1}6p^1$
$4f^25f$	6.14−1	$4d^{-1}4f^15s^15f^{-1}$	2.38−2	$4f^{-1}5p^25f^{-1}$	1.52−2	$4d^{-2}4f^2$	8.16−3	$4d^{-1}4f^15d^15f^{-1}$
	4.27−3	$4d^{-1}5d^1$	1.41−3	$4p^{-1}5p^1$	1.10−3	$4d^{-1}5g^1$	9.73−4	$4d^{-1}4f^15f^{-1}5g^1$
	8.02−4	$4p^{-1}4f^1$	7.22−4	$4f^{-1}5f^1$	6.58−4	$4f^15f^{-1}$	5.70−4	$4d^{-1}6d^1$
	5.13−4	$4p^{-2}4f^2$	4.81−4	$4p^{-1}4f^15p^15f^{-1}$	4.66−4	$4d^{-1}6g^1$	3.23−4	$4p^{-1}4d^{-1}4f^15g^1$
	3.21−4	$4s^{-1}5s^1$	2.89−4	$4d^{-2}5d^2$	2.79−4	$4p^{-1}4d^{-1}5p^15d^1$	2.32−4	$4d^{-1}7g^1$
$4f^25g$	1.59−1	$4d^{-1}4f^15p^15g^{-1}$	1.52−2	$4d^{-2}4f^2$	4.17−3	$4d^{-1}5d^1$	3.25−3	$4d^{-1}4f^25g^{-1}$
	2.36−3	$4d^{-1}4f^15f^15g^{-1}$	1.61−3	$4f^{-1}5p^15d^15g^{-1}$	1.38−3	$4p^{-1}5p^1$	1.02−3	$4d^{-1}5g^1$
	8.18−4	$4p^{-1}4f^1$	5.59−4	$4d^{-1}6d^1$	5.38−4	$4f^{-1}5f^1$	5.14−4	$4p^{-2}4f^2$
	4.69−4	$4d^{-1}6g^1$	4.65−4	$4d^{-1}4f^15g^{-1}6h1$	3.13−4	$4s^{-1}5s^1$	3.04−4	$4p^{-1}4d^{-1}4f^15g^1$
	2.88−4	$4d^{-2}5d^2$	2.77−4	$4p^{-1}4d^{-1}5p^15d^1$	2.33−4	$4d^{-1}7g^1$	2.01−4	$5g^{-1}6g^1$
$4f^26g$	1.52−2	$4d^{-2}4f^2$	1.28−2	$4p^{-1}4f^15s^16g^{-1}$	4.06−3	$4d^{-1}5d^1$	1.36−3	$4p^{-1}5p^1$
	1.05−3	$4d^{-1}5g^1$	1.03−3	$4f^{-1}5s^16p^16g^{-1}$	7.63−4	$4p^{-1}4f^1$	6.86−4	$4d^{-1}4f^26g^{-1}$
	5.48−4	$4d^{-1}6d^1$	5.36−4	$4d^{-1}4f^16f^16g^{-1}$	5.13−4	$4p^{-2}4f^2$	4.63−4	$4f^{-1}5f^1$
	4.26−4	$4d^{-1}6g^1$	3.20−4	$4p^{-1}4d^{-1}4f^15g^1$	3.10−4	$4s^{-1}5s^1$	2.85−4	$4d^{-2}5d^2$
	2.75−4	$4p^{-1}4d^{-1}5p^15d^1$	2.26−4	$4d^{-1}7g^1$	2.01−4	$5g^16g^{-1}$	1.80−4	$6g^{-1}7g^1$

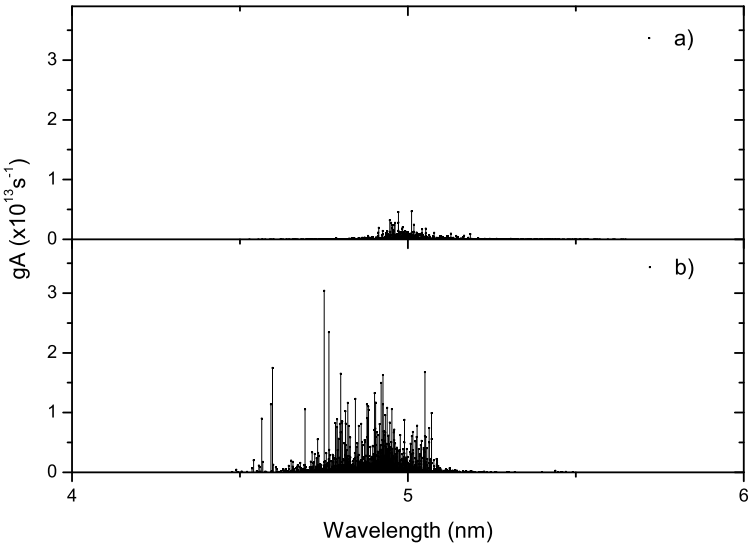

Figure 2: Calculated transition data obtained using a) single-configuration and b) configuration mixing methods for $4f^2 5d \to 4f^3$ transition in W^{25+}.

Table 2 presents configuration interaction strengths [23, 24] for $4f^3$, $4d^9 4f^4$, $4f^2 5s$, $4f^2 5p$, $4f^2 5d$, $4f^2 5f$, $4f^2 5g$, and $4f^2 6g$ configurations, which are responsible for the line formation in emission spectra of 2–30 nm range [13, 16, 39]. The largest configuration mixing is determined for $4f^2 5d$, $4f^2 5f$, and $4f^2 5g$ configurations (Table 2). Previous analysis has established that the correlation effects make a small contribution to the gA spectrum of the W^{25+} ion [13]. However, our calculations show that the CI increases the radiative transition probabilities for the $4f^2 5d \to 4f^3$ transition by an order (Fig. 2) and affects the distribution of lines. The inclusion of correlation effects changes the average wavelength and width of lines ($\bar{\lambda} = 5.02$ nm, $\sigma = 0.54$ nm to $\bar{\lambda} = 4.90$ nm, $\sigma = 1.20$ nm). Thus, the spectra from these transitions in W^{25+} have to be investigated by taking into account the configuration mixing. It is interesting to note that the strongest mixing of $4d^9 4f^4$ configuration does not take place with $4f^2 5d$ configuration. The configuration interaction strength shows that $4d^8 4f^4 5d$ and $4d^7 4f^6$ configurations have the largest influence to the $4d^9 4f^4$ configuration. The additional CI basis has been used to estimate the impact of these configurations ($4d^8 4f^4 5d$,

$4d^7 4f^6$, $4p^5 4d^9 4f^5$) on the wavelengths and radiative transition probabilities of $4d^9 4f^4 \rightarrow 4f^3$ transition. It was found that the transition wavelengths increase by less than 0.17 nm while the radiative transition probabilities change by less than 20 % for the strongest lines.

Table 3: The five major spontaneous radiative transition probabilities A^r (in s^{-1}) from each level having the largest lifetimes are presented. Arrow marks the final level to which radiative transition happens from the level. The sum of all radiative probabilities from the corresponding level is given in the last column. $a \pm b = a \times 10^{\pm b}$.

Initial level	A^r (s^{-1})	final level	A^r (s^{-1})	final level	A^r (s^{-1})	final level	A^r (s^{-1})	final level	A^r (s^{-1})	final level	$\sum A^r$ (s^{-1})
2	2.908+2	→ 1									2.908+2
4	2.125+2	→ 2	3.613−4	→ 1							2.125+2
5	3.552+2	→ 1	5.387+1	→ 2	3.015−6	→ 4					4.091+2
6	6.176+1	→ 3	6.280−2	→ 1	1.685−7	→ 5					6.182+1
7	9.194+1	→ 4	7.306−5	→ 2							9.194+1
8	7.810+1	→ 3	1.021+0	→ 6							7.912+1
9	3.703+1	→ 1	1.324+1	→ 5	2.801+0	→ 6	3.169−3	→ 2	9.071−6	→ 3	5.308+1
10	3.954+1	→ 3	2.493+0	→ 6	8.852−1	→ 1	2.228−1	→ 9	1.633−2	→ 8	4.316+1
11	1.114+2	→ 6	2.820+1	→ 1	1.375+1	→ 5	1.048+1	→ 10	8.532+0	→ 9	1.726+2
12	2.338+2	→ 5	7.144+1	→ 2	5.331+1	→ 1	3.649+1	→ 9	2.009−1	→ 11	3.952+2
13	1.813+2	→ 5	1.133+2	→ 2	1.065+2	→ 4	1.732+0	→ 1	4.639−2	→ 12	4.029+2
14	4.712+2	→ 2	1.109+2	→ 4	6.329−2	→ 1	1.203−3	→ 7	1.066−3	→ 5	5.822+2
15	3.031+2	→ 8	1.648+2	→ 6	8.315+1	→ 3	3.671+0	→ 10	2.564−3	→ 9	5.547+2
16	2.139+2	→ 10	1.166+2	→ 9	9.157+1	→ 6	4.024+0	→ 5	1.756+0	→ 11	4.312+2
17	1.944+2	→ 3	1.018+2	→ 8	4.165−1	→ 15	1.112−2	→ 10	2.230−3	→ 6	2.966+2
18	1.360+2	→ 5	1.334+2	→ 11	6.105+1	→ 2	4.338+1	→ 9	4.797+0	→ 12	3.844+2
19	2.822+2	→ 4	2.359+2	→ 7	2.083+1	→ 14	1.528−3	→ 2	3.645−5	→ 13	5.389+2
20	1.318+2	→ 3	5.609+1	→ 10	4.214+1	→ 6	3.839+1	→ 11	1.694+1	→ 9	2.920+2
21	5.476+1	→ 4	1.777+1	→ 18	1.767+1	→ 5	1.605+1	→ 1	1.489+1	→ 13	1.365+2
22	1.558+2	→ 8	2.554+1	→ 10	7.869+0	→ 20	7.033+0	→ 17	2.628+0	→ 3	2.010+2
23	2.175+2	→ 9	9.525+1	→ 8	6.324+1	→ 15	5.260+1	→ 10	2.712+1	→ 6	4.905+2
24	3.813+2	→ 12	1.119+2	→ 16	9.024+1	→ 11	5.966+1	→ 13	2.964+1	→ 2	7.139+2
25	1.737+2	→ 13	8.124+1	→ 18	6.860+1	→ 5	2.709+1	→ 1	1.325+1	→ 21	3.826+2
26	8.403+1	→ 15	6.532+1	→ 22	5.031+1	→ 8	3.473+1	→ 17	4.625−1	→ 10	2.353+2
27	4.311+2	→ 15	2.191+2	→ 17	2.177+2	→ 6	5.601+1	→ 20	2.948+1	→ 10	9.938+2
28	9.272+1	→ 14	7.731+1	→ 7	3.507+1	→ 13	2.866+1	→ 4	1.835+1	→ 21	2.870+2
29	1.584+2	→ 20	3.727+1	→ 23	1.311+1	→ 16	1.252+1	→ 18	1.088+1	→ 11	2.538+2
30	3.985+2	→ 14	2.121+2	→ 19	6.305+1	→ 4	2.850+1	→ 7	5.054−2	→ 2	7.022+2
31	2.155+2	→ 16	9.201+1	→ 11	8.567+1	→ 18	7.530+1	→ 13	2.629+1	→ 21	5.651+2
32	1.863+2	→ 19	5.689+1	→ 7	7.065−1	→ 30	2.982−2	→ 4	6.163−3	→ 14	2.439+2
33	3.112+2	→ 11	2.763+2	→ 20	2.397+2	→ 10	1.311+2	→ 22	9.485+1	→ 15	1.376+3
34	3.113+2	→ 23	2.414+2	→ 22	1.260+2	→ 26	1.070+2	→ 15	7.341+1	→ 17	8.973+2
35	3.340+2	→ 25	2.618+2	→ 18	6.399+1	→ 12	5.837+1	→ 14	5.116+1	→ 24	9.161+2
36	3.681+2	→ 18	2.599+2	→ 12	1.387+2	→ 16	1.097+2	→ 33	8.845+1	→ 29	1.102+3

Continued on next page

Table 3: (continued)

Initial level	A^r (s^{-1})	final level	A^r (s^{-1})	final level	A^r (s^{-1})	final level	A^r (s^{-1})	final level	A^r (s^{-1})	final level	$\sum A^r$ (s^{-1})
37	3.591+2	→ 11	2.570+2	→ 27	2.377+2	→ 29	1.013+2	→ 33	9.612+1	→ 10	1.304+3
38	1.856+2	→ 21	1.109+2	→ 31	9.051+1	→ 24	8.616+1	→ 11	2.971+1	→ 13	5.600+2
39	1.010+2	→ 31	9.077+1	→ 6	6.030+1	→ 10	5.205+1	→ 20	3.895+1	→ 29	4.116+2
40	6.083+2	→ 33	5.372+2	→ 29	3.206+2	→ 39	2.216+2	→ 38	1.390+2	→ 18	2.291+3
41	3.458+2	→ 39	3.151+2	→ 36	1.407+2	→ 20	1.015+2	→ 33	9.812+1	→ 27	1.461+3
172	1.814+1	→ 163	5.520+0	→ 32	3.331+0	→ 7	9.091−1	→ 19	2.132−2	→ 30	2.792+1
204	1.451+2	→ 172	4.946+1	→ 163	1.353+1	→ 32	1.029+1	→ 19	1.787+0	→ 30	2.216+2
222	8.664+1	→ 172	2.509+1	→ 204	7.509+0	→ 32	3.216−4	→ 163	2.847−6	→ 199	1.192+2
242	2.567+2	→ 32	9.733+1	→ 199	4.496+1	→ 163	3.558+1	→ 204	1.602+1	→ 19	5.005+2
248	1.982+1	→ 222	3.057−4	→ 172	6.850−6	→ 204	3.217E−10	→ 242			1.982+1
260	3.697+2	→ 204	9.626+1	→ 163	7.476+1	→ 172	6.964+1	→ 199	4.832+1	→ 222	7.065+2
284	1.021+2	→ 222	6.843+1	→ 242	3.351+1	→ 248	1.895+1	→ 172	1.101+1	→ 32	2.387+2
348	3.282+2	→ 260	2.211+2	→ 270	1.363+2	→ 242	6.810+1	→ 284	5.298+1	→ 255	8.931+2
350	2.059+2	→ 222	1.724+2	→ 248	2.040+1	→ 284	5.335−3	→ 204	1.537−3	→ 172	3.987+2
366	1.611+2	→ 248	5.406+1	→ 297	1.384+1	→ 260	1.298+1	→ 172	5.480+0	→ 284	2.516+2
368	1.025+3	→ 32	2.482+2	→ 222	8.422+1	→ 260	5.449+1	→ 284	5.195+1	→ 7	1.674+3
392	7.199+2	→ 32	2.098+2	→ 7	1.274+2	→ 222	1.071+2	→ 260	6.180+1	→ 331	1.613+3
493	5.645+2	→ 350	3.231+2	→ 248	2.727+2	→ 366	1.379+2	→ 32	8.289+1	→ 368	1.625+3
4247	1.734+3	→ 248	1.212+1	→ 4130	3.621+0	→ 350	2.497+0	→ 366	1.638+0	→ 222	1.755+3
4796	9.590+2	→ 248	8.271+2	→ 350	4.071+2	→ 4247	9.289+1	→ 4130	7.794+1	→ 222	2.397+3
4956	1.340+2	→ 248	3.454+1	→ 4247	1.098+1	→ 4796	9.944−1	→ 350	3.145−4	→ 4130	1.805+2

Electron-impact excitations from the long lived levels are responsible for the population of levels in a low density plasma. Table 3 presents levels, which have the smallest values of the total radiative decay rates. We only present levels with the total radiative transition rates not exceeding the total decay rates of the ground configuration levels. It should be noted that the second excited level can decay to the ground level only through the magnetic octupole transition ($\lambda = 2790.29$ nm) which has not been studied here. The highly-excited states of the ion have radiative lifetimes comparable with the lifetimes of the excited levels of the ground configuration which decay mainly through the weak magnetic dipole transitions. These levels belong to the $4d^9 4f^4$ and $4d^8 4f^5$ configurations. The extremely large total angular momentum J values of these levels limit the possible decay channels and lead to the large lifetimes.

The previous investigations [13, 16, 39] show that the lines from the electric dipole $(n = 4) \rightarrow (n = 4)$, $(n = 5) \rightarrow (n = 4)$, and $(n = 5) \rightarrow (n = 5)$ transitions in W^{25+} ion have wavelengths in the 2 – 30 nm region. The

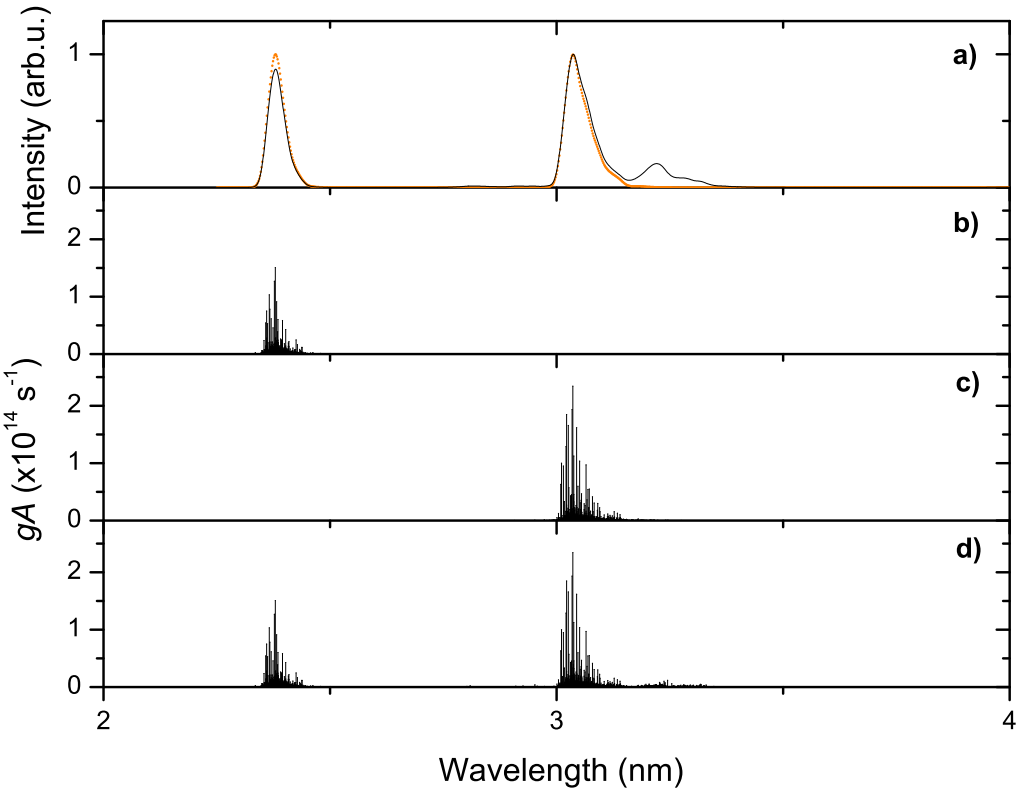

Figure 3: Calculated transition data for W^{25+} in the 2 – 4 nm range. a) Convoluted gA spectra with a full width at half maximum of 0.02 nm. Orange line corresponds to the summed contribution from b) $4f^2 6g \rightarrow 4f^3$ and c) $4f^2 5g \rightarrow 4f^3$ transitions. Black line comes from d) spectrum of all transitions considered in this work.

lines in the range from 2 to 4 nm have been identified as corresponding to $4f^{N-1}5g \rightarrow 4f^N$ (W^{20+}–W^{27+}) and $4f^{N-2}5s5g \rightarrow 4f^{N-1}5s$ (W^{20+}–W^{26+}) transitions [13, 39]. The study [39] has included $4f^{N-2}5s5g \rightarrow 4f^{N-1}5s$ transition because the first excited configurations of the considered ions cannot combine radiatively with the ground configuration. However, correlation effects open the decay channels for electric dipole transitions as it is demonstrated above for the W^{25+} ion. Furthermore, the levels of $4f^2 5s$ configuration do not have the largest lifetimes among the investigated levels.

Figures 3, 4, and 5 show theoretical radiative transition probabilities multiplied by the statistical weights of initial levels. The strongest lines in the spectra are concentrated at 2.4, 3.0, and 5.0 nm. The first two groups of the

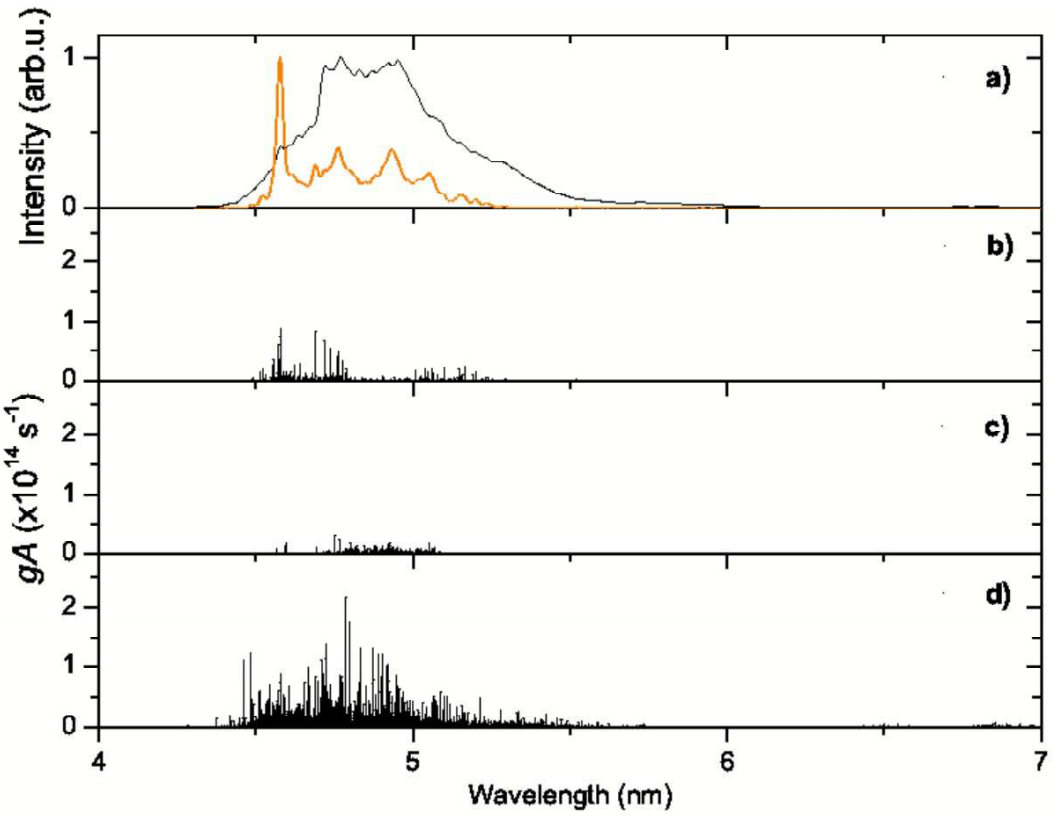

Figure 4: Calculated transition data for W^{25+} in the 4 – 7 nm range. a) Convoluted gA spectra with a full width at half maximum of 0.02 nm. Orange line corresponds to the summed contribution from b) $4d^9 4f^4 \rightarrow 4f^3$ and c) $4f^2 5d \rightarrow 4f^3$ transitions. Black line comes from d) spectrum of all transitions considered in this work.

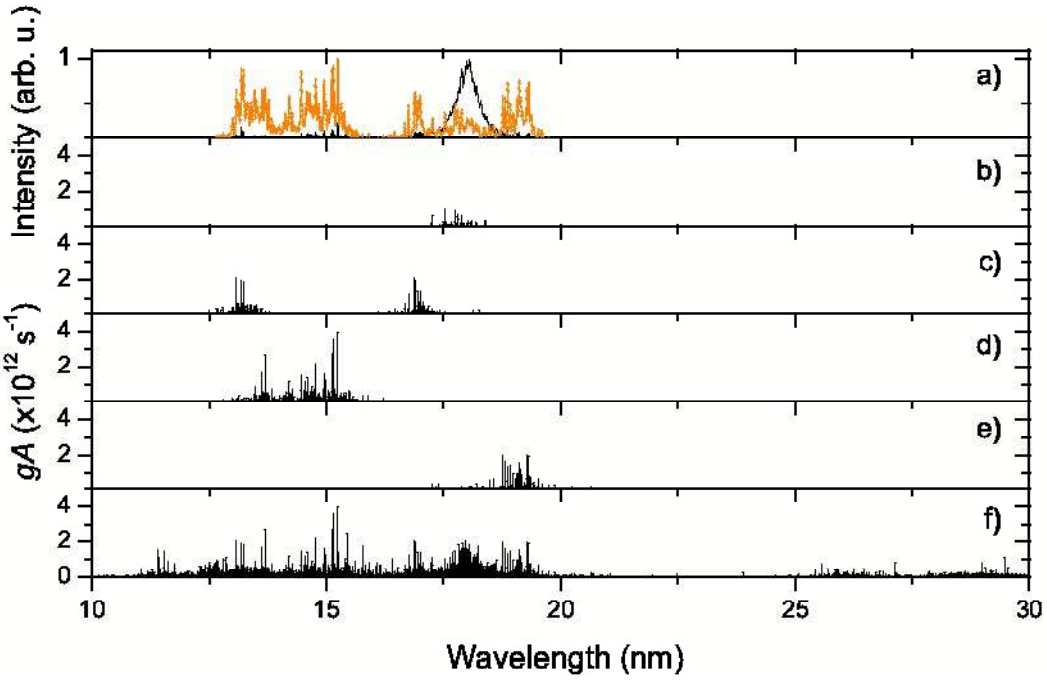

Figure 5: Calculated transition data for W^{25+} in the 10 – 30 nm range. a) Convoluted gA spectra with a full width at half maximum of 0.02 nm. Orange line corresponds to the summed contribution from b) $4f^2 5p \rightarrow 4f^2 5s$; c) $4f^2 5d \rightarrow 4f^2 5p$; d) $4f^2 5f \rightarrow 4f^2 5d$, and e) $4f^2 5g \rightarrow 4f^2 5f$ transitions. Black line comes from f) spectrum of all transitions considered in this work.

lines correspond mainly to $4f^2 6g \rightarrow 4f^3$ and $4f^2 5g \rightarrow 4f^3$ transitions. The additional peaks at 3.22 nm arise from the electric dipole $4d^9 4f^3 5p \rightarrow 4f^3$ transitions. Those lines from $4f^2 5g \rightarrow 4f^3$ and $4d^9 4f^3 5p \rightarrow 4f^3$ transitions have been already identified in large helical device plasmas with the wavelengths $\lambda = 3.09$ nm and $\lambda = 3.25$ nm, respectively [11]. The identification is based on the data from [3] where the Unresolved Transition Array (UTA) approximation is used in calculations (3.09, 3.24 nm). However, the UTA calculations provide the mean wavelengths slightly higher compared to the peak values due to the asymetric nature of gA spectra of these transitions. The UTA mean wavelengths calculated using the pseudorelativistic approach [13] provides similar values (3.11, 3.22 nm) in comparison to the experimental wavelengths of corresponding peaks. Our wavelengths (3.04, 3.22 nm) are shorter than the experimental ones. On the other hand, gA values for $4d^9 4f^3 5p \rightarrow 4f^3$ transition are about six times smaller than those for $4f^2 5g \rightarrow 4f^3$ transition. Therefore, it is unlikely that $4d^9 4f^3 5p \rightarrow 4f^3$ transition would influence the line formation in the observed spectra. Lines corresponding to $4f^2 5g \rightarrow 4f^3$ transition have been also observed in [17] but their observed wavelength $\lambda = 3.10$ nm is slightly longer compared with the previous value of 3.09 nm [11]. On the other hand, our calculations show that one of their unidentified lines with $\lambda = 2.41$ nm [17] belongs to the $4f^2 6g \rightarrow 4f^3$ transition for which gA values have a peak at 2.38 nm. This transition is not considered in [39] assuming that high n, l states would be collisionally destroyed in a dense laser produced plasma.

The third group of lines at 5.0 nm originates from $4d^9 4f^4 \rightarrow 4f^3$ and $4f^2 5d \rightarrow 4f^3$ transitions with the large contribution from $4d^8 4f^5 \rightarrow 4d^9 4f^4$ transition (Fig. 4). From the energy level spectrum (Fig. 1) one can see that $4f^2 5d$ and $4d^9 4f^4$ configurations overlap. The width of $4f^2 5d$ configuration is about few times smaller than the width of $4d^9 4f^4$ configuration. Since wavelengths of the strongest lines from $4d^9 4f^4 \rightarrow 4f^3$, and $4f^2 5d \rightarrow 4f^3$ transitions concentrate in the same area (Fig. 4b and 4c), it suggests that the transitions take place from the same energetic region.

Region of 10–30 nm is covered by lines which originate from $4f^2 5g \rightarrow 4f^2 5f$, $4f^2 5f \rightarrow 4f^2 5d$, $4f^2 5d \rightarrow 4f^2 5p$, $4f^2 5p \rightarrow 4f^2 5s$, $4d^9 4f^3 5p \rightarrow 4d^9 4f^3 5s$, $4f^2 6d \rightarrow 4f^2 5f$, and $4f 5p 5d \rightarrow 4f 5p^2$ transitions in W^{25+} (Fig. 5). The obtained results agree well with the other calculations [16]. Large transition probabilities for the lines near 18 nm correspond mainly to $4d^9 4f^3 5p \rightarrow 4d^9 4f^3 5s$ transitions.

4. The modeling of emission spectra

Many strong transitions fall into the range of 2 – 30 nm where strong emission from the considered configurations is observed (Figs. 3, 4, and 5). Intensive lines in the low-density plasma mainly originate from the configurations which correspond to the one-electron excitations from the configuration levels with the large lifetimes because such levels are mainly populated. We have calculated the electron-impact excitation cross-sections from the ground $4f^3_{5/2}$ subconfiguration in the distorted-wave approximation at 790 eV electron beam energy, which corresponds to the energy used in EBIT measurements [6]. The single-configuration approximation and the UTA mode implemented in Flexible Atomic Code (FAC) [40] were applied. It is determined that the strongest one-electron excitations, in decreasing order, are: $4d \rightarrow 4f$, $4d \rightarrow 5d$, $4f \rightarrow 5g$, $4f \rightarrow 5f$, $4d \rightarrow 5g$, $4f \rightarrow 6g$, $4d \rightarrow 5p$. The electron-impact cross-sections for $4d \rightarrow 4f$ excitation are by one order larger compared with $4d \rightarrow 5d$ excitation and by two orders larger than $4f \rightarrow 5d$ excitation. It can be seen from Figs. 3, 4, and 5 that transitions from $4d^9 4f^4$, $4f^2 5p$, $4f^2 5d$, $4f^2 5f$, $4f^2 5g$, and $4f^2 6g$ configurations feature large radiative transition probabilities. However, the large radiative transition probabilities alone are not enough to ensure strong lines in the spectrum of **a** low-density plasma. The distribution of gA values will not fully reproduce the spectral shape and important transitions, since it does not take population mechanisms into account.

As far as we know, no modeling of the spectra for W^{25+} has been performed for a monoergetic electron beam, except in [41]. Their collisional-radiative modeling included $4f^3$ and $4f^2 5l$ ($l = 0, 1, 2, 3$) configurations but omitted $4d^9 4f^4$ and $4f^2 5g$ configurations. However, the configuration interaction strengths presented in Table 2 show that $4f^2 5d$ configuration strongly mixes with $4d^9 4f^4$ configuration. Furthermore, the configuration interaction has to be taken into account between $4f^2 5f$ and $4d^9 4f^3 5s$ configurations. On the other hand, $4d^9 4f^4$, $4d^9 4f^3 5d$, and $4f^2 5g$ configurations have to be included into modeling due to their strong electron-impact excitations from the ground configuration.

In this work, the corona model is used to estimate population of levels and to find contribution of various transitions to the line formation for W^{25+} in a low-density plasma. The population of levels from the higher levels through radiative cascade is also included in our investigation. Two approaches are adopted to obtain electron-impact excitation rates. First of all, the rates

are considered as being proportional to the electric multipole (E1, E2, E3) transition probabilities, and the corona model is used to find the population of levels. Then these spectra are compared with the modeling where the electron-impact excitation rates are calculated using the distorted-wave (DW) approximation.

For large incident electron energies, compared with excitation energies, the plane-wave Born (PWB) method produces accurate electron-impact excitation rates but this method is restricted only to spin-allowed transitions [31]. On the other hand, the intermediate coupling mixes states with the various spins and the total spin quantum number is not well defined. At this energy limit, radiative transition probabilities can be used instead of electron-impact excitation cross-sections, because the matrix element of the PWB operator transforms to the matrix elements of electric multipole transition operators. Thus, the selection rules for the PWB cross-sections are identical to those for the electric multipole radiation. The previous study of W^{29+} to W^{37+} spectra in EBIT plasma [10] has demonstrated that relative line intensities for resonant $4p^5 4d^{N+1} + 4p^6 4d^{N-1} 4f \rightarrow 4p^6 4d^N$ $(N = 1 - 9)$ transitions quite well agree with the collisional-radiative modeling [6], but in the case when electric dipole transition probabilities are used in the corona model.

In addition, the electron-impact excitation rates from the levels of the ground configuration are calculated within the distorted-wave approximation at 790 eV of electron beam energy and 10^{12} cm^{-3} of electron beam density using the FAC code. The same basis of interacting configurations is employed in these calculations. The Gaussian distribution function with a full width at half-maximum of 30 eV is used for the electron energy.

Good agreement between both approaches can be noticed for groups of lines which correspond to transitions from the excited configurations $4f^2 6g$, $4f^2 5g$ (Fig. 6), $4d^9 4f^4$, and $4f^2 5d$ (Fig. 7) to the ground configuration. Some discrepancies between two applied approaches can be attributed to the different methods implemented in the GRASP2K and FAC codes. However, the relative intensities determined by the different approaches for the group of lines at 2.4 nm differ by two times. It can be explained by the fact that the relative excitation rates from the levels of the ground configuration to the levels of $4f^2 6g$ and $4f^2 5g$ configurations differ when the PWB and DW approximations used. Spectra of gA values show good agreement with modeled spectra too. It should be noted that the influence of $4f^2 5d \rightarrow 4f^3$ transition to the formation of lines in the 4–7 nm range drastically increases

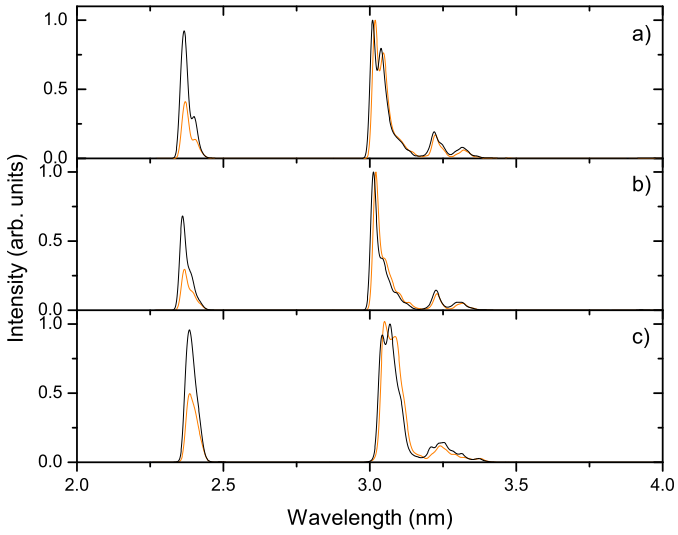

Figure 6: Spectra from corona models in the 2 – 4 nm range when populations of levels are obtained after excitation from a) the ground, b) the first excited, and c) the second excited levels. Black line - spectrum when electric dipole transition probabilities used for electron-impact excitation rates; orange line - electron-impact excitation rates calculated using DW method.

in the both modeled spectra (Fig. 7). Many strong lines correspond to this transition while the corresponding gA values are much smaller compared with those from the $4d^9 4f^4 \rightarrow 4f^3$ transition.

The largest discrepancies among the spectra of two corona models and gA values are obtained in the 10–30 nm range where $(n = 5) \rightarrow (n = 5)$ transitions are observed (Fig. 8). The radiative cascade plays a crucial role in the line formation for the transitions in both corona models. The radiative cascade has the largest influence for the lowest configurations of the complex.

Corona modeling, where the DW excitations are used to calculate populations of the excited levels, especially highlights the lines from the $4f^2 5f \rightarrow 4f^2 5d$ transition in the 13 nm region. This contrasts to the line intensities detemined using the modeling with electric transition probabilities. Interestingly, the intensities of the strongest lines obtained with the DW method are not strongly affected by radiative cascade. In the PWB limit, the initial configuration is mainly populated through the radiative cascade because direct excitations from the levels of the ground configuration are very weak. On the other hand, electron-impact excitation cross-sections from the ground

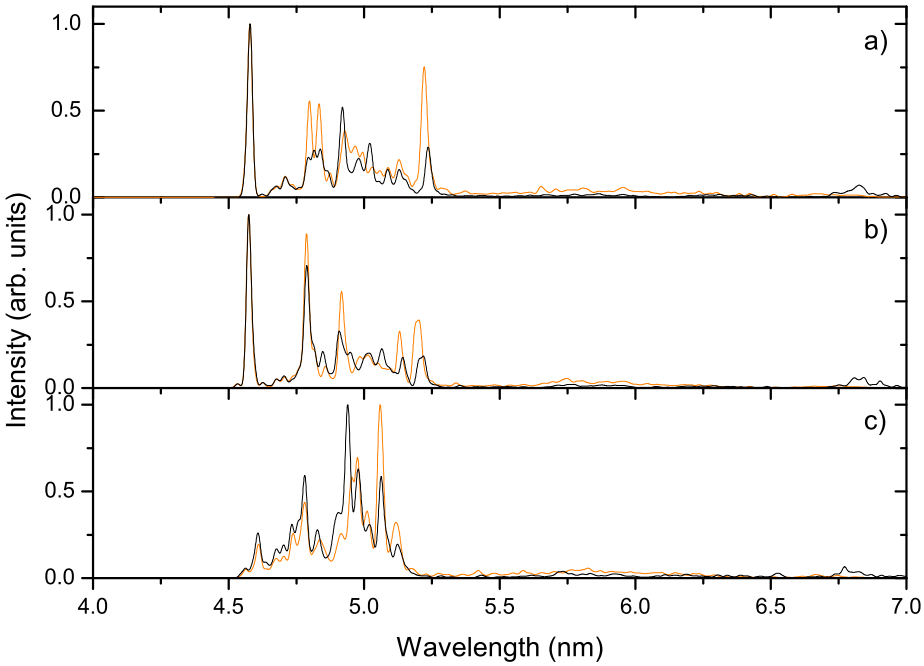

Figure 7: Same as Fig. 6 but the 4 – 7 nm range.

configuration to the $4f^2 5f$ configuration are quite strong according to our UTA calculations performed using the DW approximation. The same region is populated by the lines from $4f^2 5d \rightarrow 4f^2 5p$ transition. However, in this case the influence of the radiative cascade is very important.

The strongest increase of line intensities compared with gA spectrum is observed in the 10–12 nm region. This region is formed by the $4f^2 5s \rightarrow 4f^3$ transition which has not been investigated before. Their electric dipole transition probabilities are very small compared to other electric dipole transitions as it is mentioned in Sec 3. Only the radiative cascade from the higher levels is responsible for the strong increase of the population of levels of $4f^2 5s$ configuration.

Other groups of lines at 18 nm ($4f^2 5d \rightarrow 4f^2 5p$, $4f^2 5p \rightarrow 4f^2 5s$) and 28 nm ($4f^2 5p \rightarrow 4f^2 5s$) are strongly affected by the radiative cascade as well.

Finally, the most interesting result of modeling in the 10–30 nm range is a complex structure of lines which do not form emission bands. Those lines, close to 13, 18, and 29 nm, can be observed in EBIT plasma. Another interesting study would be in the wavelength range of the 10–12 nm where

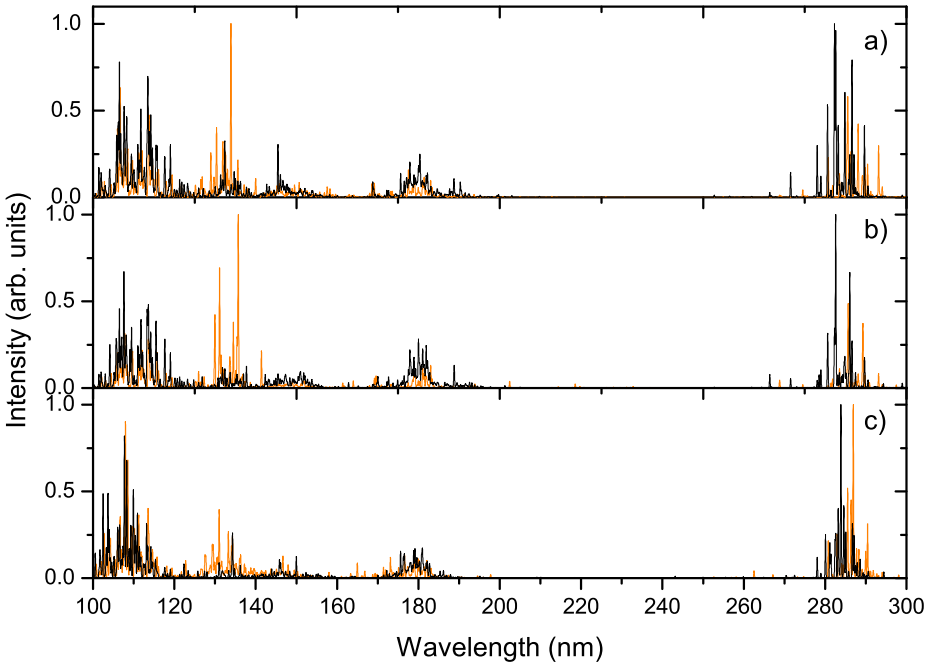

Figure 8: Same as Fig. 6 but the 10 – 30 nm range.

lines from the $4f^2 5s \rightarrow 4f^3$ transitions are concentrated. These transitions were not previously analyzed neither theoretically nor experimentally.

5. Estimation of uncertainties

Estimation of uncertainties in our data is based on the difference between single-configuration and CI methods. Because our CI basis includes the main configurations important for the considered configurations, we assume that the larger CI basis will not have larger impact to the energy levels, wavelengths, and transition probabilities.

For $4f^3$ configuration, the energy levels are approximately 0.23 a.u. lower in CI calculations compared with the single-configuration method. Even better agreement is obtained for $4f^2 5s$ (0.045 a.u.) and $4f^2 5p$ (0.014 a.u.) configurations. Large mixing among the configuration state functions of $4d^9 4f^4$ and $4f^2 5d$ configurations indicates that these levels have to be investigated together. For this group of configurations, the disagreement between both calculations does not reach 0.2 a.u. The largest discrepancies appear for the

more excited configurations of $n = 5$ complex ($4f^2 5f$ - 0.312 a.u., $4f^2 5g$ - 0.570 a.u.).

Due to different uncertainties for various configurations, the uncertainties for wavelengths differ for various transitions. The smallest discrepancy is detemined for $4f^2 6g \to 4f^3$ (0.06 nm) and $4f^2 5g \to 4f^3$ (0.12 nm) transitions. The largest discrepancies up to 0.5 nm take place for $4f^2 5g \to 4f^2 5f$ and $4f^2 5f \to 4f^2 5d$ transitions. Furthermore, the agreement between both methods is within 0.3 nm for $4f^2 5d \to 4f^2 5p$ and $4f^2 5p \to 4f^2 5s$ transitions, and within 0.2 nm for $4d^9 4f^4 + 4f^2 5d \to 4f^3$ transitions.

Radiative transition probabilities obtained using single-configuration and CI methods do not differ by more than 30 % for many $4f^2 6g \to 4f^3$, $4f^2 5g \to 4f^3$, $4f^2 5g \to 4f^2 5f$, and $4f^2 5p \to 4f^2 5s$ transitions. Similar uncertainties can be attributed to transitions which include $4f^2 5d$, and $4d^9 4f^4$ configurations: $4f^2 5f \to 4f^2 5d$, $4f^2 5d \to 4f^2 5p$, and $4d^9 4f^4 + 4f^2 5d \to 4f^3$.

6. Conclusions

We have analyzed energy levels and radiative transition probabilities in the W^{25+} ion using the multiconfiguration Dirac-Fock method and the extended basis of configurations. Our calculations show that lifetimes of some $4d^9 4f^4$ and $4d^8 4f^5$ configuration levels are comparable with the lifetimes of levels from the ground configuration where mostly magnetic dipole transitions are available.

In addition, correlation effects have been studied using configuration interaction strength in the configurations responsible for the formation of the strongest lines in the spectrum. We have determined that the correlation effects are crucial for some configurations and transitions. The largest mixing of configurations takes place for $4f^2 5d$, $4f^2 5f$, and $4f^2 5g$ configurations. Influence of the correlations has been studied for the $4f^2 5s \to 4f^3$ and $4f^2 5d \to 4f^3$ transitions. The configuration interaction allows the electric dipole transitions from the first excited $4f^2 5s$ configuration to the ground $4f^3$ configuration. However, the electric dipole transition probabilities are approximately six orders larger than those of the electric octupole transitions. For the $4f^2 5d \to 4f^3$ transition, it was found that the correlation effects increase the electric dipole transition probabilities by an order of magnitude, the width of the spectrum becomes wider approximately by two times, and the average wavelength shifts to the shorter wavelength side.

The corona model is used to find contribution of various transitions to the formation of lines in the spectrum. The modeling has demonstrated good agreement with the spectra of gA values for strong transitions to the ground configuration. However, the corona modeling boosts intensities of the lines corresponding to the $4f^2 5s \rightarrow 4f^3$ transition. Levels of the $4f^2 5s$ configuration are mainly populated through radiative cascade from higher levels.

Two approaches are applied to estimate electron-impact excitation rates in the corona model – the distorted-wave approximation and radiative transition probabilities used for the electron-impact excitation rates. Good agreement is determined between two approaches for strong transitions in the 2 – 7 nm range. Modeling of spectra in the 10–30 nm range reveals the structure of lines which do not merge to emission bands. We suggest further EBIT observations for those lines in W^{25+} spectra.

Akcnowledgement

This research was funded by European Social Fund under the Global Grant Measure (No.: VP1-3.1-ŠMM-07-K-02-015).

References

1. Isler R, Neidigh R, Cowan R. Tungsten radiation from tokamak-produced plasmas. *Physics Letters A* 1977;**63** (3): 295–97.

2. Hinnov E, Mattioli M. Observations of multiply ionized tungsten radiation in the PLT discharges. *Physics Letters A* 1978;**66** (2): 109–11.

3. Finkenthal M, Huang LK, Lippmann S, Moos HW, Mandelbaum P, Schwob JL, Klapisch M. Soft X-ray bands of highly ionized tungsten, gold and lead emitted by the TEXT tokamak plasma. *Physics Letters A* 1988;**127** (5): 255–58.

4. Fournier KB. Atomic data and spectral line intensities for highly ionized tungsten (Co-like W^{47+} to Rb-like W^{37+}) in a high-temperature, low-density plasma. *At. Data Nucl. Data Tables* 1998;**68** (1): 1–48.

5. Biedermann C, Radtke R, Schwob JL, Mandelbaum P, Doron R, Fuchs T, Fußmann G. EUV Spectroscopy of Highly Charged Tungsten Ions Relevant to Hot Plasmas. *Physica Scripta* 2001;**T92**: 85-88.

6. Radtke R, Biedermann C, Schwob JL, Mandelbaum P, Doron R. Line and band emission from tungsten ions with charge 21+ to 45+ in the $45 - 70$ Å range. *Phys. Rev. A* 2001;**64** (1): 012720.

7. Utter SB, Beiersdorfer P, Trabert E. Electron-beam ion-trap spectra of tungsten in the EUV. *Canadian Journal of Physics* 2002;**80** (12): 1503–15.

8. Pütterich T, Neu R, Biedermann C, Radtke R, ASDEX Upgrade Team. Disentangling the emissions of highly ionized tungsten in the range 4 – 14 nm. *J. Phys. B: At. Mol. Opt. Phys.* 2005;**38** (16): 3071–82.

9. Ralchenko Y, Reader J, Pomeroy JM, Tan JN, Spectra of W^{39+}–W^{47+} in the 12–20 nm region observed with an EBIT light source. *J. Phys. B: At. Mol. Opt. Phys.* 2007;**40** (19): 3861–75.

10. Jonauskas V, Kučas S, Karazija R. On the interpretation of the intense emission of tungsten ions at about 5 nm. *J. Phys. B: At. Mol. Opt. Phys.* 2007;**40** (11): 2179–88.

11. Chowdhuri MB, Morita S, Goto M, Nishimura H, Nagai K, Fujioka S. Line analysis of EUV Spectra from Molybdenum and Tungsten Injected with Impurity Pellets in LHD. *Plasma Fusion Res.* 2007;**2**: S1060.

12. Pütterich T, Neu R, Dux R, Whiteford AD, O'Mullane MG. Modelling of measured tungsten spectra from ASDEX Upgrade and predictions for ITER. *Plasma Physics and Controlled Fusion* 2008;**50** (8): 085016.

13. Harte CS, Suzuki C, Kato T, Sakaue HA, Kato D, Sato K, Tamura N Sudo S, D'Arcy R, Sokell E, White J, O'Sullivan G. Tungsten spectra recorded at the LHD and comparison with calculations. *J. Phys. B: At. Mol. Opt. Phys.* 2010;**43** (20): 205004.

14. Clementson J, Beiersdorfer P, Magee EW, McLean HS, Wood RD. Tungsten spectroscopy relevant to the diagnostics of ITER divertor plasmas. *Journal of Physics B: Atomic, Molecular and Optical Physics* 2010;**43** (14): 144009.

15. Ralchenko Y, Draganic IN, Osin D, Gillaspy JD, Reader J. Spectroscopy of diagnostically important magnetic-dipole lines in highly charged $3d^n$ ions of tungsten. *Phys. Rev. A* 2011;**83** (3): 032517.

16. Suzuki C, Harte CS, Kilbane D, Kato T, Sakaue HA, Murakami I, Kato D, Sato K, Tamura N Sudo S, Goto M, D'Arcy R, Sokell E, O'Sullivan G. Interpretation of spectral emission in the 20 nm region from tungsten ions observed in fusion device plasmas. *Journal of Physics B: Atomic, Molecular and Optical Physics* 2011;**44** (14): 175004.

17. Podpaly YA, Rice JE, Beiersdorfer P, Reinke ML, Clementson J, Barnard HS. Tungsten measurement on Alcator C-Mod and EBIT for future fusion reactors. *Can. J. Phys.* 2011;**89** (5): 591-597.

18. Bogdanovich P, Kisielius R. Theoretical energy level spectra and transition data for $4p^6 4d$, $4p^6 4f$ and $4p^5 4d^2$ configurations of W^{37+}ion. *At. Data Nucl. Data Tables* 2012;**98** (4): 557–65.

19. Bogdanovich P, Kisielius R. Theoretical energy level spectra and transition data for $4p^6 4d^2$, $4p^6 4d4f$ and $4p^5 4d^3$ configurations of W^{36+}ion. *At. Data Nucl. Data Tables* 2013;**99** (5): 580–94.

20. Madeira T, Amorim P, Parente F, Indelicato P, Marques J. Analysis of the quasicontinuum band emitted by highly ionised tungsten atoms in the 4 –7nm range. *Eur. Phys. J. D* 2013;**67** (1): 1–6.

21. Kramida A, Shirai T. Energy levels and spectral lines of tungsten, W III through W LXXIV. *At. Data Nucl. Data Tables* 2011;**95** (3): 305–474.

22. Kramida A. Recent progress in spectroscopy of tungsten. *Can. J. Phys.* 2009;**89** (5): 551–570.

23. Karazija R. *Introduction to the Theory of X-Ray and Electronic Spectra of Free Atoms*. Plenum Press; New York 1996.

24. Kučas S, Jonauskas V, Karazija R. Global characteristics of atomic spectra and their use for the analysis of spectra. IV. Configuration interaction effects. *Physica Scripta* 1997;**55** (6): 667–675.

25. Jonauskas V, Kisielius R, Kynienė A, Kučas S, Norrington PH. Magnetic dipole transitions in $4d^n$ configurations of tungsten ions. *Phys Rev A* 2010;**81**: 012506.

26. Jonauskas V, Gaigalas G, Kučas S. Relativistic calculations for M1-type transitions in configurations of W^{29+} – W^{37+} ions. *At. Data Nucl. Data Tables* 2012;**98** (1): 19–42.

27. Kynienė A, Jonauskas V, Kučas S, Karazija R. On the existence of dipole satellites in the region of M2,3-L2,3 non-dipole emission lines for transition elements. *Lithuan. J. Phys.* 2008;**48**: 219.

28. Jonauskas V, Karazija R, Kučas S. The essential role of many-electron Auger transitions in the cascades following the photoionization of 3p and 3d shells of Kr. *J. Phys. B: At. Mol. Opt. Phys.* 2008;**41** (21): 215005.

29. Palaudoux J, Lablanquie P, Andric L, Ito K, Shigemasa E, Eland JHD, Jonauskas V, Kučas S, Karazija R, Penent F. Multielectron spectroscopy: Auger decays of the krypton 3d hole. *Phys. Rev. A* 2010; **82** (4): 043419.

30. Jonauskas V, Kučas S, Karazija R. Auger decay of 3p-ionized krypton. *Phys. Rev. A* 2011;**84** (5): 053415.

31. Cowan RD. *The Theory of Atomic Structure and Spectra*. Berkeley, CA: University of California Press; 1981.

32. Gaigalas G, Rudzikas Z, Gaidamauskas E, Rynkun P, Alkauskas A. Pecularities of spectroscopic properties of W^{24+}. *Phys. Rev. A* 2010;**82** (1): 014502.

33. Gaigalas G, Rudzikas Z, Rynkun P, Alkauskas A. Dependence of the probabilities of the electric-multipole electron transitions in W^{24+} on multipolarity. *Phys. Rev. A* 2011;**83** (3): 032509.

34. Jönsson P, Gaigalas G, Bieroń J, Froese Fischer C, Grant IP. New version: Grasp2K relativistic atomic structure package. *Comput. Phys. Commun.* 2013;**184** (9): 2197–2203.

35. Jonauskas V, Masys Š, Kynienė A, Gaigalas G. Cascade emission in electron beam ion trap plasma. *J. Quant. Spectrosc. Radiat. Transfer* 2013;**127**: 64–69.

36. Beiersdorfer P, Schweikhard L, Crespo Lopez-Urrutia JR, Widmann K. The magnetic trapping mode of an electron beam ion trap: New opportunities for highly charged ion research. *Review of Scientific Instruments*. 1996;**67** (11): 3818–26.

37. Beiersdorfer P, Olson RE, Brown GV, Chen H, Harris CL, Neill PA, Schweikhard L, Utter SB, Widmann K. X-Ray Emission Following Low-Energy Charge Exchange Collisions of Highly Charged Ions. *Phys. Rev. Lett.*. 2000;**85** (24): 5090–93.

38. Beiersdorfer P, Bitter M, Marion M, Olson RE. Charge-exchange-produced K-shell x-ray emission from Ar^{16+} in a tokamak plasma with neutral-beam injection. *Phys. Rev. A* 2005;**72** (3): 032725.

39. Harte CS, Higashiguchi T, Otsuka T, D'Arcy R, Kilbane D, O'Sullivan G. Analysis of tungsten laser produced plasmas in the extreme ultraviolet (EUV) spectral region. *J. Phys. B: At. Mol. Opt. Phys.* 2012;**45** (20): 032725.

40. Gu MF. The flexible atomic code. *Can. J. Phys.* 2008;**86** (5): 675–89.

41. Radtke R, Biedermann C, Fussmann G, Schwob J, Mandelbaum P, Doron R. Measured line spectra and calculated atomic physics data for highly charged tungsten ions. *Atomic and Plasma - Material Interaction Data for Fusion* 2007;**13**:45–66.